RESEARCH ARTICLE | MARCH 01 2023

A quasi-one-dimensional model for the stagnation streamline in hypersonic magnetohydrodynamic flows

Special Collection: Hypersonic Flow

Kai Luo (罗凯) ; Qiu Wang (汪球) ; Jinping Li (李进平) ; Wei Zhao (赵伟); Sangdi Gu (顾桑迪)

Physics of Fluids 35, 036101 (2023)
https://doi.org/10.1063/5.0138366

Physics of Fluids ARTICLE scitation.org/journal/phf

A quasi-one-dimensional model for the stagnation streamline in hypersonic magnetohydrodynamic flows

Cite as: Phys. Fluids **35**, 036101 (2023); doi: 10.1063/5.0138366
Submitted: 11 December 2022 · Accepted: 10 February 2023 ·
Published Online: 1 March 2023

View Online Export Citation CrossMark

Kai Luo (罗凯),[1] Qiu Wang (汪球),[1,a)] Jinping Li (李进平),[1] Wei Zhao (赵伟),[1] and Sangdi Gu (顾桑迪)[2]

AFFILIATIONS

[1]State Key Laboratory of High Temperature Gas Dynamics, Institute of Mechanics, Chinese Academy of Sciences, No. 15 Beisihuanxi Road, Beijing 100190, China
[2]Department of Aeronautical and Aviation Engineering, The Hong Kong Polytechnic University, Kowloon, Hong Kong, China

Note: This paper is part of the special topic, Hypersonic Flow.
[a)]**Author to whom correspondence should be addressed:** wangqiu@imech.ac.cn

ABSTRACT

The flow near the stagnation streamline of a blunt body is often attracted and analyzed by using the approximation of local similarity, which reduces the equations of motion to a system of ordinary differential equations. To efficiently calculate the stagnation-streamline parameters in hypersonic magnetohydrodynamic (MHD) flows, an improved quasi-one-dimensional model for MHD flows is developed in the present paper. The Lorentz force is first incorporated into the original dimensionally reduced Navier–Stokes equations to compensate for its effect. Detailed comparisons about the shock standoff distance and the stagnation point heat flux are conducted with the two-dimensional Navier–Stokes calculations for flows around the orbital reentry experiment model, including gas flows in thermochemical nonequilibrium under different magnetic field strengths. Results show that the shock curvature should be considered in the quasi-one-dimensional model to prevent accuracy reduction due to the deviation from the local similarity assumption, particularly for hypersonic MHD flows, where the shock standoff distance will increase with larger magnetic strength. Then, the shock curvature parameter is introduced to compensate for the shock curvature effect. A good agreement between the improved quasi-one-dimensional and the two-dimensional full-field simulations is achieved, indicating that the proposed model enables an efficient and reliable evaluation of stagnation-streamline quantities under hypersonic MHD flows.

I. INTRODUCTION

Magnetohydrodynamics (MHD) is the study of the magnetic properties and behavior of electrically conducting fluids, which plays an important role in several branches of physics, such as solar physics. Researchers started to take note of the potential of MHD for aerodynamics in the late 1950s and early 1960s,[1–3] in principle to utilize magnetic fields to control and optimize the flowfield of the vehicle. Considerable attention has also been paid to the hypersonic flows with the ionization of the air since then. When a vehicle travels through the atmosphere at high-enough speeds, a strong bow shock forms around the vehicle forebody which compresses the freestream to very high temperatures. Given the ionization and consequent electrical conductivity associated with air at such high temperatures, it is natural to consider electromagnetic control for this class of flows, herein called MHD flow control.

As an active thermal protection technique for hypersonic flight vehicles, MHD has attracted intense interest due to recent improvements in electromagnetic technology and superconductors. In MHD flow control, applying a magnetic field to weakly ionized plasma flow around a reentry vehicle induces electric currents in the shock layer. The interaction between the electric current and the magnetic field generates the Lorenz force, which decelerates the plasma flow in the shock layer. Consequently, the shock layer is expanded and the convective heat flux to the vehicle is mitigated via MHD flow control. The feasibility of applying magnetic technologies to hypersonic vehicles and propulsion systems has already been preliminary proved through some experiments and numerical simulations.[2–5] However, due to the complexity of MHD technology, its research is still in the exploratory stage, and many fundamental issues remain to be addressed. Experimental methods are critical for the development of MHD flow control. Due to the high enthalpy required to ensure that the test flow has adequate conductivity, only certain wind tunnels worldwide can be used for these experiments.[3,6–11] Moreover, the presence of the electromagnetic field also results in substantial difficulties in performing flow diagnostics. Hence, current research on MHD flow control primarily focus on numerical simulations, including formulating different numerical schemes for solving the MHD equations[12–14] and evaluating the MHD effect for different magnetic fields and flight trajectories.[15,16]

Flow field analysis around the nose tip and leading edge of hypersonic vehicles has attracted the most interest because the largest heat flux occurs in these regions. Thus, this is the primary focus of the current work. Evaluating the effectiveness of MHD flow control is typically conducted by applying a magnetic field and investigating the heat flux mitigation at the stagnation points. However, the calculation of the stagnation streamline flow in hypersonic flows around spheres and cylinders requires solving the governing equations with two independent spatial variables. The computational domain must be extended at least beyond the boundaries of the subsonic region of the shock layer. Although this is not particularly difficult, it is rather time-consuming and not suitable for parametric studies. On the other hand, the computational time can be significantly reduced if only the flow equations at the stagnation streamline are solved.

Several researchers have attempted to solve the flow field along the stagnation streamline of a blunt body in supersonic and hypersonic flows without a magnetic field. Additional equations or estimations are added to close the equations by estimating the momentum equation in the circumferential direction.[17–22] One typical approach among them, called dimensionally reduced Navier–Stokes equations (DRNSE), is based on the local similarity in the stagnation streamline region.[23] Klomfass and Müller[24] first used modern computational fluid dynamics algorithms to solve the conservative form of the DRNSE approximated by Kao.[23] William *et al.*[25] adopted the shock-capturing method to solve the DRNSE along the stagnation streamline of a sphere. The results showed that the shock standoff distance at the stagnation point predicted by the dimensionally reduced 1D equations was about 10% shorter than that obtained by the original 2D/axisymmetric equations. A similar result was observed by Klomfass and Müller.[24] Lee[26] proposed a boundary condition based on the shock wave angle in the vicinity of the stagnation streamline and the correlation with the shock shape. This method improved the accuracy of predicting the shock standoff distance. Nevertheless, the quasi-one-dimensional Navier–Stokes equations for hypersonic MHD flows have yet to be very extensively researched.

This study proposes a quasi-one-dimensional model to predict the flow along the stagnation line in hypersonic MHD flows. The DRNSE is solved by applying the finite difference method. The Lorentz force is first added to the DRNSE, and the shock curvature parameter is incorporated to improve the method's accuracy. Numerical computations assuming a low magnetic Reynolds number are conducted for hypersonic flow over the orbital reentry experiment (OREX) model. The DRNSE is validated by a detailed comparison with the two-dimensional flow calculations using the same physical models. The proposed high-efficiency model can be used to investigate the overall quantitative behavior of physical–chemical phenomena in hypersonic MHD flows.

II. DERIVATION OF THE QUASI-ONE-DIMENSIONAL MODEL FOR MHD FLOWS

A. Ansatz for DRNSE

The typical MHD flow pattern is shown in Fig. 1. It is consistent with the traditional blunt flow and characterized by the free stream,

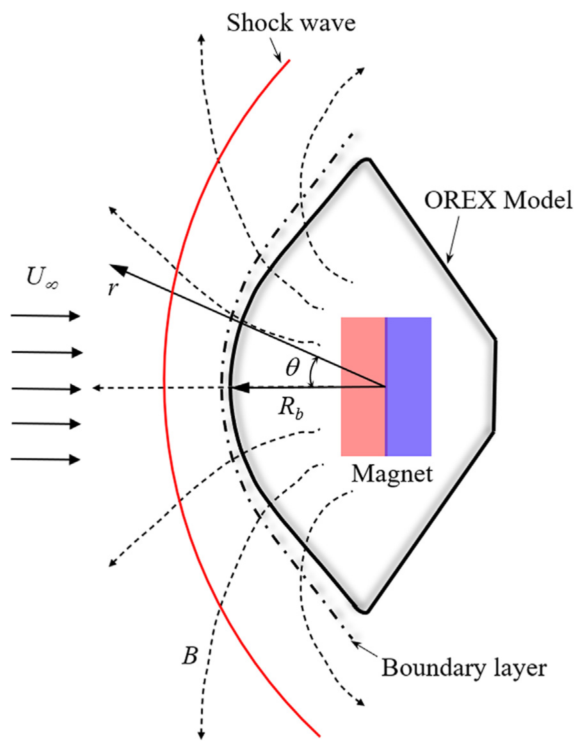

FIG. 1. Schematic diagram of hypersonic MHD flow over a blunt body.

post-shock inviscid region, and boundary layer. Subscript ∞ represents the properties of the free stream, subscript b represents the properties immediately after the detached bow shock, and subscript w represents the properties at the wall to identify the flow regions defined by the freestream and the wall. r and θ are the radial and polar coordinates of the physical space in Fig. 1, respectively. R_b is the nose radius, U_∞ is the velocity of freestream, and B is the magnetic induction vector. As mentioned in Sec. I, researchers often focus only on a local region instead of the entire flow field around a hypersonic vehicle due to the computational complexity. It has been shown that the flow along the stagnation streamline of a blunt body can be analyzed using the quasi-one-dimensional Navier–Stokes equations. Therefore, it is beneficial to develop a stagnation streamline model to conduct parametric studies or rapid analyses of a specific flow situation for hypersonic MHD flows over blunt bodies.

The quasi-one-dimensional model is indeed derived from the Navier–Stokes equations with MHD interaction based on the low magnetic Reynolds number model,[27] and we also try to use the entire axisymmetric simulation to validate our quasi-one-dimensional model. Thus, the regular nonequilibrium Navier–Stokes under the spherical coordinate system (r, θ, φ) for MHD flows are also shown in Appendix A in detail, which is also validated by typical test cases in Appendix E. In addition, the electrical conductivity model that we apply is added in Appendix B.

The present paper aims to develop a quasi-one-dimensional approximation for the stagnation streamline under MHD flows, where the simplified set of equations are mainly based on the dimensionally reduced Navier–Stokes equations (DRNSE) for hypersonic flows without a magnetic field. We first introduce the strategy of the DRNSE and then describe the modified DRNSE for hypersonic MHD flows. Local similarity is embedded in a systematic scheme of successive approximations by expanding the flow quantities based on the distance from the stagnation point to derive the DRNSE along the stagnation streamline for symmetric flows. The symmetry of the flow field implies that the radial velocity u, pressure p, translational–rotational temperature T, the vibrational temperature T_v, and mass fraction of species x_s are symmetric to the axis $\theta = 0$. In contrast, the angular velocity component v behaves anti-symmetric. Additionally, the Newtonian theory provides a useful approximation for the surface pressure in the hypersonic limit, i.e., when $Ma \gg 1$,[28]

$$p_w - p_\infty = \rho_\infty U_\infty^2 \cos^2\theta. \tag{1}$$

The separation of variables technique is applied to a suitable set of flow quantities, and it will be expanded in an asymptotic expansion. Then, the flow variables are expanded about the axis of symmetry with respect to $\sin\theta$ as below,[24] and the treatment of the pressure term refers to Eq. (1),

$$\begin{aligned} u(r,\theta) &= u_1(r)\cos\theta + u_2(r)\cos\theta\sin^2\theta + \cdots, \\ v(r,\theta) &= v_1(r)\sin\theta + v_2(r)\sin^3\theta + \cdots, \\ T(r,\theta) &= T_1(r) + T_2(r)\sin^2\theta + \cdots, \\ T_v(r,\theta) &= T_{v,1}(r) + T_{v,2}(r)\sin^2\theta + \cdots, \\ x_s(r,\theta) &= x_{s,1}(r) + x_{s,2}(r)\sin^2\theta + \cdots, \\ p(r,\theta) - p_\infty &= p_1(r)\cos^2\theta + p_2(r)\cos^2\theta\sin^2\theta + \cdots. \end{aligned} \tag{2}$$

Then, only the terms corresponding to the first truncation in Eq. (2) are preserved, and the higher order terms are ignored. Therefore, the flow quantities can be represented as follows:

$$\begin{aligned} u &= u_1(r)\cos\theta, \\ v &= v_1(r)\sin\theta, \\ T &= T_1(r), \\ T_v &= T_{v,1}(r), \\ x_s &= x_{s,1}(r), \\ p &= p_\infty + p_1(r)\cos^2\theta. \end{aligned} \tag{3}$$

The origin coordinate is set at the center point of the sphere. It then follows that the boundary conditions are expressed as follows:

Freestream $r \to \infty$,

$$\begin{aligned} u_1 = -U_\infty, \quad v_1 = U_\infty, \quad p_1 = 0, \quad T_1 = T_\infty, \\ T_{v,1} = T_{v,\infty}, \quad x_{s,1} = x_{s,\infty}. \end{aligned} \tag{4}$$

Stagnation point $r \to R_b$,

$$\begin{aligned} u_1 = 0, \quad v_1 = 0 \quad \text{or} \quad \frac{\partial v_1}{\partial r} = 0, \quad x_{s,1} = x_{s,w} \quad \text{or} \quad \frac{\partial x_{s,1}}{\partial r} = 0, \\ \frac{\partial p_1}{\partial r} = 0, \quad T_1 = T_{v,1} = T_w \quad \text{or} \quad \frac{\partial T_1}{\partial r} = \frac{\partial T_{v,1}}{\partial r} = 0. \end{aligned} \tag{5}$$

Different wall boundary conditions, including a no-slip or slip wall, an isothermal or adiabatic wall, and a full catalytic or noncatalytic wall, can be chosen in the ansatz.

Notably, the above approximations are suitable for symmetric flow problems, where an axisymmetric magnetic field distribution is necessary to keep the flow axisymmetric. Fortunately, a dipole magnet is axisymmetric and is frequently used. For hypersonic MHD flows, the Lorentz force F_L is also introduced with an applied magnetic field. The interaction between the magnetic field and the azimuthal electric current induces the Lorentz force in the shock layer, as shown in Fig. 2, where the flowfield is obtained using the axisymmetric simulation method shown in Appendix A. The results indicate that Lorentz force decelerates the plasma flow in the shock layer and pushes the bow shock wave away from a space vehicle,

$$\rho_\infty U_\infty^2 A\cos^2\theta = F = \left(p_w - p_\infty + \int_{r_w}^{r_\infty} F_{L,r}\,dr\right)A, \tag{6}$$

$$p_w = p_\infty + \rho_\infty U_\infty^2 \cos^2\theta - \int_{r_w}^{r_\infty} F_{L,r}\,dr. \tag{7}$$

In hypersonic flows without a magnetic field, the pressure is expressed in Eq. (3), which originates from the Newtonian theory approximation.[28] From the Newton's second law, the time rate of change of momentum is equal to the force $\boldsymbol{F}$ exerted on the control volume, and $\boldsymbol{F}/A$ is the difference of the surface pressure of the control volume, i.e., $\boldsymbol{F}/A = p_w - p_\infty$, and A is the surface area as illustrated in Fig. 3. For hypersonic MHD flows, the radial Lorentz force $F_{L,r}$ is also acting on the fluid elements as sketched in Fig. 3, which will subsequently affect the pressure on the surface. The Lorentz force is a volume force, like the centrifugal force used to correct the Newtonian theory for a curved surface. Accordingly, the Lorentz force is incorporated into the Newtonian theory as shown in Eq. (6), where the Lorentz force is integrated along the whole streamline from the stagnation point to the far freestream part, i.e., from point 1 to point 2 as sketched in Fig. 3. Then, the pressure at the stagnation point can be obtained as shown in Eq. (7), where the Lorentz force is also considered to compensate for its effect. In other words, the strategy of Lorentz force consideration in the Newtonian theory is the same as

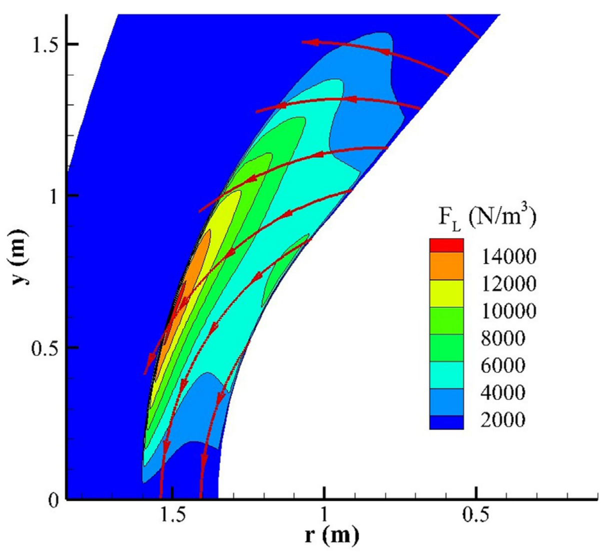

FIG. 2. Two-dimensional distribution of the Lorentz force for the parameter; orbital reentry experiment model in Japan, $R_b = 1.35$ m, $B_0 = 0.5$ T, and $U_\infty = 5561$ m/s.

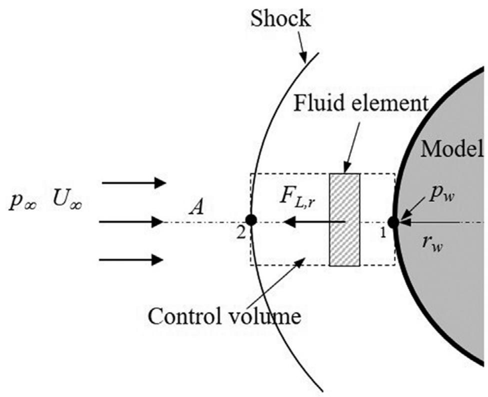

FIG. 3. Schematic diagram of Lorentz force corrections to Newtonian theory.

treatment of centrifugal force corrections to Newtonian theory for curved surfaces.[28] Notably, the unit of $F_{L,r}$ in the following equations is N/m^3, i.e., the force per unit volume,

$$p = p_\infty + p_1(r)\cos^2\theta - \int_r^{r_\infty} F_{L,r}dr. \tag{8}$$

Subsequently, the approximate pressure distribution in Eq. (3) along the stagnation line is then corrected as shown in Eq. (8). Except for the pressure term, the other parameter distributions as shown in Eq. (3) are kept the same.

The tangential pressure gradient in the tangential momentum equation is expressed from Eq. (8) as follows:

$$\frac{\partial p}{\partial \theta} = -2p_1(r)\cos\theta\sin\theta - \int_r^{r_\infty} \frac{\partial F_{L,r}}{\partial \theta}dr. \tag{9}$$

The radial Lorentz force can be found in Eq. (A5) and is also expressed here as below:

$$F_{L,r} = \sigma\left(-B_\theta^2 u + B_\theta B_r v\right), \tag{10}$$

where B_r and B_θ are the strength of magnet field in the r and θ direction, respectively. σ is the electrical conductivity, which is defined in Appendix B.

The above relations are then substituted into the two-dimensional NS equations in spherical coordinates, which are shown in Eq. (A1). In the resulting expressions, the terms with coefficients $\sin\theta$ or higher powers of $\sin\theta$ can be ignored since they are small compared to the remaining terms because $\theta \to 0$ and $\cos\theta$ equals to 1. This constraint produces the modified DRNSE for hypersonic MHD flow, which is expressed formally as Eq. (11). More details on the DRNSE for non-MHD hypersonic flows are given by Klomfass and Müller,[24]

$$\frac{\partial \boldsymbol{Q}}{\partial t} + \frac{\partial \boldsymbol{F}}{\partial r} + \boldsymbol{H} = \frac{\partial \boldsymbol{F}_v}{\partial r} + \boldsymbol{H}_v + \boldsymbol{S}_{\text{Flow}} + \boldsymbol{S}_{MHD}, \tag{11}$$

where t is time; $\boldsymbol{Q}$ is the vector of the conservative variables; $\boldsymbol{F}$ and $\boldsymbol{H}$ are the inviscid flux vector; $\boldsymbol{F}_v$ and $\boldsymbol{H}_v$ are the viscous flux vector; $\boldsymbol{S}_{\text{Flow}}$ is the chemical source term; And $\boldsymbol{S}_{MHD}$ is a source term associated with the MHD effects. Detailed formulas of these vectors are shown in Appendix C.

In the above equation, the factor is also factorized in the equation of the angular momentum to simplify the two-dimensional equations at the stagnation line. The terms with the coefficients $\sin\theta$ or higher powers of $\sin\theta$ are ignored. Thus, $\sin\theta$ will disappear directly in the DRNSE equations without magnetic fields. However, an additional term, $F_{L,r}/\sin\theta$, will appear in Eq. (C1) while the Lorentz force is introduced. Although the radial Lorentz force is 0 everywhere on the stagnation streamline when $\theta \to 0$, as also depicted in Fig. 2 under a dipole magnetic field, the additional term $F_{L,r}/\sin\theta$ cannot be ignored directly, where both $F_{L,r}$ and $\sin\theta$ approach 0 at the stagnation line. Thus, the influence of the Lorentz force should be considered particularly when deriving the quasi-one-dimensional model for MHD flows.

B. Numerical procedures

In the present study, the same thermochemical reaction model as the two-dimensional calculation was used for the quasi-one-dimensional model. For the chemical reaction model, the following seven chemical species, N, O, N_2, O_2, NO, NO^+, and e^-, were considered. We adopted Dunn and Kang's model,[29] a finite rate chemical kinetic model that includes 18 chemical reactions. In addition, Park's two-temperature model[30] is employed to consider the thermal nonequilibrium state of gas. The transport coefficients, such as the effective diffusion coefficient of each species, the mixture viscosity, the mixture translational–rotational thermal conductivity, and the mixture vibrational electron thermal conductivity, are evaluated using Blottner's curve fitting model with Wilke's mixing rule.[31,32] The vibrational-electron-electronic energy E_v includes the vibrational and electric excitation energies of atoms and molecules. The terms of the energy exchange processes include vibrational–translational energy relaxation, electronic-translational energy relaxation, and vibrational energy loss due to dissociation.[33–35] It is assumed that the other modes have negligible effects.

In the following discussions, 1D represents the quasi-one-dimensional simulation (DRNSE) for hypersonic MHD flows, and 2D represents the entire axisymmetric simulation.

The 1D simulation results were validated by comparison with the 2D simulation results; the same numerical algorithms are used for both. The governing equations were solved using a finite difference approach. The convective terms were approximated using the AUSMPW+ scheme,[36] and the central difference method was applied to the viscous terms. Time integration was performed in the 1D simulation by applying the Runge–Kutta method. The only difference to the 1D simulation is that the time integration was performed using the lower–upper symmetric Gauss–Seidel (LU-SGS) scheme[37] for the 2D simulations. The grid and related resolution study are given in Appendix F.

C. Calculation conditions

The OREX capsule launched by Japan in 1994 (Ref. 38) is utilized as the calculation model. Its configuration and the computational region are shown in Fig. 4. OREX has an axisymmetric two-dimensional shape, and its nose radius is 1.35 m. Other details can be found in Ref. 3. The freestream conditions and wall temperature are listed in Table I. They correspond to the OREX flight conditions at altitudes of 55.7, 59.6, and 63.6 km. The chemical composition of the

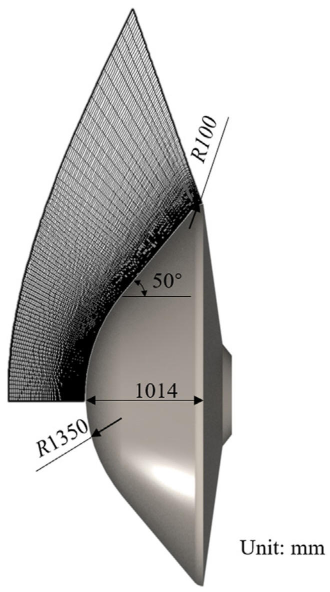

FIG. 4. Configuration of OREX and the calculation region.

freestream gas is assumed to be 79% N_2 and 21% O_2 by the mass fraction at the respective altitude

$$B_r = B_0 \frac{R_b^3}{2r^3}\cos\theta, \quad B_\theta = B_0 \frac{R_b^3}{2r^3}\sin\theta. \tag{12}$$

The externally applied magnetic field around OREX is produced by a dipole magnet, which is frequently used in ground MHD experiments or numerical simulations.[10,39] The magnetic field's distribution uses the dipole field which was defined in Eq. (12), where R_b is the nose radius, and B_0 is the strength of the magnetic field at the stagnation point. For the permanent magnets, the magnetic field strength is generally less than 0.8 T. Thus, different magnetic fields ($B_0 = 0$–0.7 T) are selected for examining the influence of the strength of the applied magnetic field on the proposed MHD flow control method.

No-slip, noncatalytic, and fixed wall temperature conditions are used as the boundary conditions on the wall surface. The translational–rotational temperature and vibrational electron temperature on the wall surface are assumed to be in equilibrium with the wall temperature, as listed in Table I.

D. Comparison of 1D and 2D results

The most prominent phenomenon in the MHD flow is the shock standoff distance Δ, which increases after applying the magnet field, and the stagnation point heat flux q_w decreases. However, this study does not focus on evaluating the effectiveness of MHD flow control; instead, we conduct validation and improvement of the proposed quasi-one-dimensional stagnation streamline model under MHD flow. The shock standoff distance and stagnation point heat flux are chosen as the key parameters for our investigations.

TABLE II. Comparison of the stagnation point heat flux and shock standoff distance between the 1D and 2D simulation for case 2.

		0 T	0.3 T	0.5 T	0.7 T
Δ (m)	1D	0.087	0.125	0.219	0.347
	2D	0.095	0.142	0.259	0.412
	Deviation	8.4%	12.0%	15.4%	15.7%
q_w (kW/m^2)	1D	254.61	226.16	211.49	201.36
	2D	263.26	230.16	209.28	200.00
	Deviation	3.3%	1.7%	1.1%	0.7%

It is expected in the simplified 1D calculation that the flow field properties along the stagnation streamline agree well with the results of the entire flow field calculation, i.e., the 2D simulation in this study. A detailed comparison between the 1D and 2D simulations is conducted, and the results are shown in Table II and Fig. 5. As the magnetic field B_0 increases from 0 to 0.7 T, the shock standoff distance increases, and the stagnation point heat flux decrease. It is shown in Table II that the stagnation point heat flux is similar for the 1D and 2D simulations for all cases, with the largest deviation of 3.3% at $B_0 = 0$ T. Due to the simulation complexity of aerodynamic heating, the 3.3% discrepancy is acceptable. In contrast, there are significant differences in the shock standoff distance between the 1D and 2D simulations in all cases. The values for the 1D simulations are smaller than the 2D simulations, about 8.4% smaller at $B_0 = 0$ T (without a magnetic field) and 15.7% smaller at $B_0 = 0.7$ T. Therefore, the larger the magnetic field, the larger the shock standoff distance is, and the larger the deviation between the 1D and 2D is. William[25] found that the shock standoff distance at the stagnation point predicted by the DRNSE was about 10% shorter than that obtained by the original 2D/axisymmetric equations, which is in line with the results of the present study ($B_0 = 0$ T). Unfortunately, the application of a magnetic field to the MHD flow increases this deviation. Subsequently, we are investigating the underlying mechanism that leads to this deviation.

The flow properties along the stagnation streamline for the 1D and 2D calculations are shown in Figs. 6 and 7. The objective is to determine if the simplification term in the 1D model causes deviations. The radial coordinate is normalized using the radius of the sphere (R_b) and the shock standoff distance (Δ), i.e., $\bar{r} = \frac{r-R_b}{\Delta}$. The trends of the density, pressure, translational temperature, and radial velocity show

TABLE I. Freestream conditions and wall temperature.

Case	Altitude h (km)	Velocity U_∞ (m/s)	Temperature T_∞ (K)	Pressure p_∞ (Pa)	Wall temperature T_w (K)
1	55.7	4759.1	258.74	39.48	1571
2	59.6	5561.6	248.12	23.60	1519
3	63.6	6223.4	237.14	14.02	1413

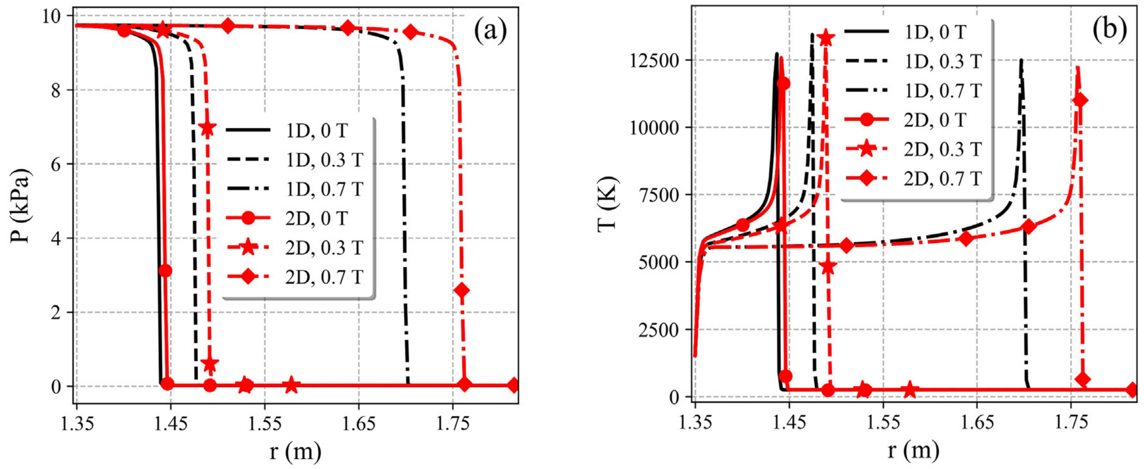

FIG. 5. Comparison of flow properties along the stagnation streamline between 1D and 2D under case 2: (a) Pressure and (b) temperature.

excellent agreements between the 1D and 2D calculations at all strengths of the magnetic field. However, there are significant differences in the tangential velocity gradient along the stagnation line as shown in Fig. 7, especially for regions close to the bow shock. 1D-shock curvature (SC) represents the improved model, which will be discussed in detail in Sec. III. The tangential velocity gradient is larger for the 1D than the 2D calculations for most regions between the shock and the wall, i.e., the mass flow rate in the tangential direction is larger for the 1D than the 2D calculation, resulting in a smaller shock standoff distance, as shown in Table II. Nevertheless, the approximations in Eq. (3) satisfy the wall boundary conditions, especially for the pressure term which originates from the Newtonian

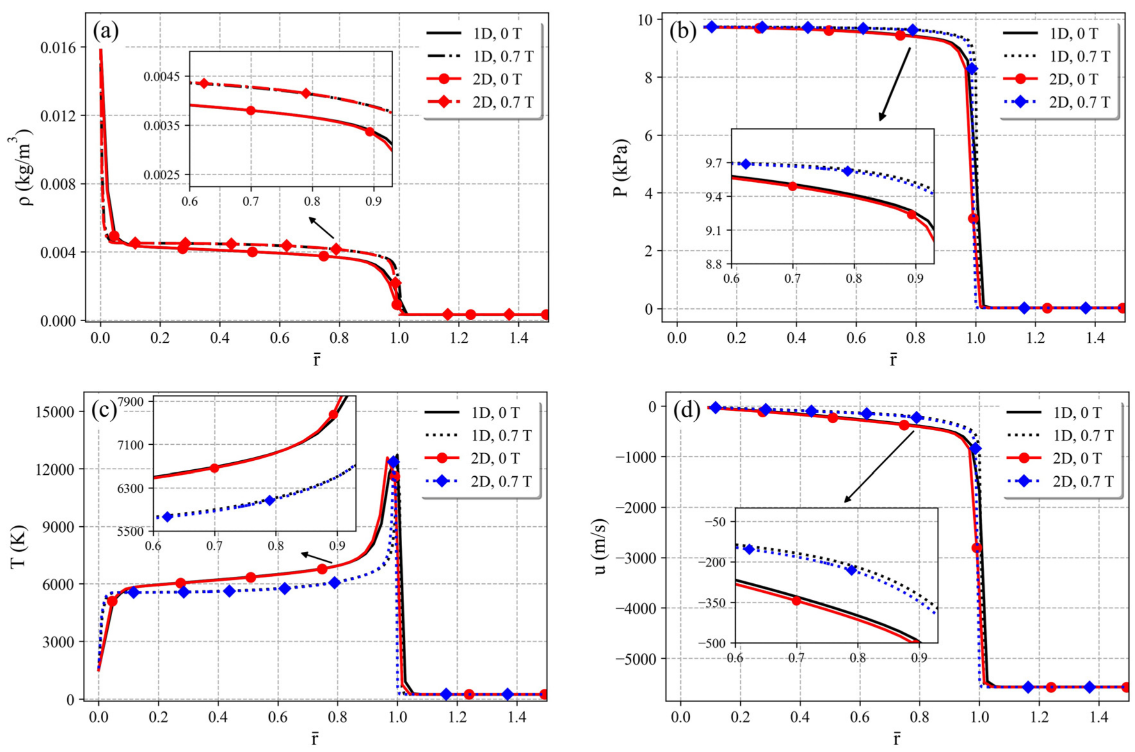

FIG. 6. Comparison of the flow properties along the stagnation streamline between the 1D and 2D simulations for case 2. (a) Density, (b) pressure, (c) translational–rotational temperature, and (d) radial velocity.

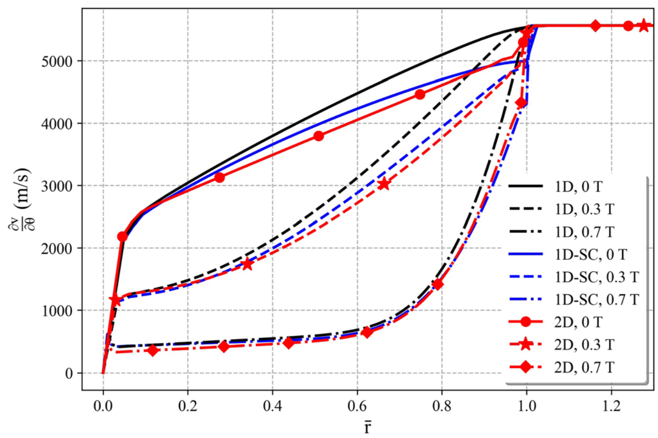

FIG. 7. The comparisons of the tangential velocity gradient for case 2.

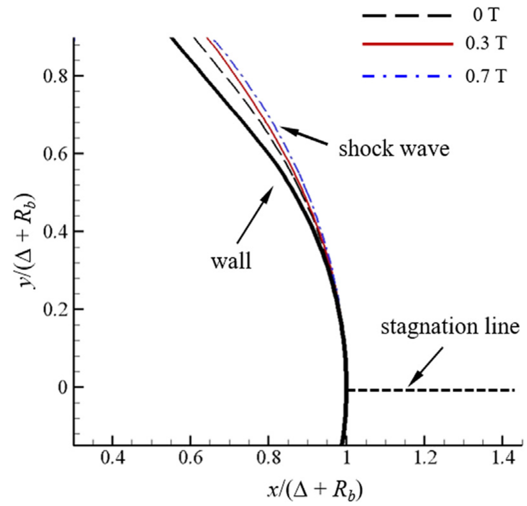

FIG. 8. Comparison of the shock wave surface and the wall. The shock wave surfaces are obtained from the 2D results for case 2.

theory at the stagnation point. Thus, we can also observe in Fig. 7 that the tangential velocity gradient between 1D and 2D shows excellent agreement in the boundary layer indeed. In other words, all the properties at the edge of the boundary layer along the stagnation streamline agree well between 1D and 2D, leading to a similar stagnation point heat flux between them as shown in Table II.

The tangential velocity gradient is an important parameter to determine the shock standoff distance of existing theories. Thus, the inaccurate estimate of tangential velocity gradient in 1D will lead to deviations of the shock standoff distance. Therefore, we explore this phenomenon in detail below and make reasonable modifications to the 1D model under hypersonic MHD flow to improve the accuracy of the 1D MHD flow simulation.

III. IMPROVED 1D MODEL FOR MHD FLOWS

To derive the quasi-one-dimensional MHD flows along the stagnation streamline, local similarity is also applied, along with the first-order truncation of the power expansion of the flow quantities. However, the local similarity is analogous to that of the flow field solution having full cylindrical or spherical symmetry, and the velocity formula in Eq. (2) is based on the assumption that the shock wave is concentric with the sphere model. Any deviation would lead to inaccuracy. Thus, the influence of the shock curvature on the 1D result should be considered because an offset exists between the shock wave and the concentric sphere. Figure 8 shows a schematic diagram comparing the shock wave and the wall close to the stagnation point region for the 2D computation with and without a magnet field. It is observed that the shock wave and the spherical model are not homocentric. The further away from the axis of symmetry or the stagnation line, the larger the deviation between the shock and the sphere wall is, even without a magnetic field ($B_0 = 0\,\mathrm{T}$). The result by Klomfass and Müller[24] also indicates that the deviation of the shock standoff distance from the DRNSE increases with the decreasing Mach number or increasing shock standoff distance (corresponding to $B_0 = 0\,\mathrm{T}$ in this study). The larger the strength of the magnetic field, the larger the deviation between the shock wave and the sphere wall is, as indicated in Fig. 8. Therefore, special attention should be paid to the influence of the shock curvature on the accuracy of the 1D simulation,

$$u = u_1(r)\cos(\theta - \beta), \quad v = v_1(r)\sin(\theta - \beta). \tag{13}$$

The above analysis has shown the existence of an angle β between the tangential velocity direction and the surface of the detached shock wave. The variable β can be determined by the shock angle α and the polar coordinate θ, i.e., $\beta = \alpha + \theta - \frac{\pi}{2}$, as shown in Fig. 9. This will lead to the less applicable of the original local similarity. Thus, a modified velocity component description along the stagnation streamline is shown in Eq. (13) where the influence of the shock curvature has been incorporated in Eq. (3) to improve the accuracy of the first-order truncation,

$$p_b = p_\infty\left[\frac{1-\gamma}{\gamma} + \frac{2\gamma}{\gamma+1}M_\infty^2\cos^2(\theta - \beta)\right]. \tag{14}$$

Similarly, the approximate pressure is also shown below. The relation of the oblique portion of the shock is expressed in Eq. (14).

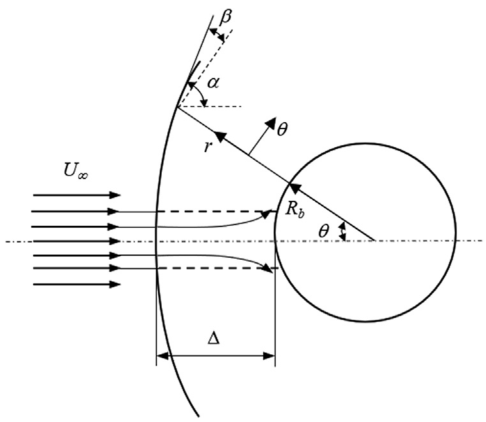

FIG. 9. Schematic diagram of the shock curvature parameter.

Combined with the surface pressure given by the Newtonian theory, the pressure at the stagnation line is defined as follows:

$$p = p_\infty + p_1(r)\cos^2(\theta - \beta) - \int_r^{r_\infty} F_{L,r}\,dr. \tag{15}$$

Since the angle β is always 0 at the stagnation streamline, it is only a function of θ, i.e., $\beta = \beta(\theta)$.

After adding the shock curvature parameter, the components of the inviscid flux $\boldsymbol{H}$, the viscous flux vectors $\boldsymbol{H}_v$, and the source term $\boldsymbol{S}_{MHD}$ in Eq. (11) are obtained again, and these specific equations are shown in Eq. (D1) in Appendix D.

For a stagnation streamline with $\theta = \beta = 0$, the incorporation of β has a negligible influence on the value of u, p, T, T_v, and x_s; however, it affects the first-order derivative of v. Meanwhile, we add a new dependent variable $\frac{\partial\beta}{\partial\theta}$ to the governing equations. The boundary conditions for this variable are as below.

Stagnation point $r = R_b$,

$$\frac{\partial\beta}{\partial\theta} = 0. \tag{16}$$

Bow shock $r = R_b + \Delta$,

$$\frac{\partial\beta}{\partial\theta} = \left(\frac{\partial\beta}{\partial\theta}\right)_b. \tag{17}$$

Thus, the value of the shock curvature parameter $\frac{\partial\beta}{\partial\theta}$ in the shock layer is between 0 and $(\frac{\partial\beta}{\partial\theta})_b$. A value of $(\frac{\partial\beta}{\partial\theta})_b = 0$ indicates a perfectly circular shock wave shape at the stagnation point of the sphere as in the original local similarity. This value was also determined to be a constant value for the whole reactive flow regime by Belouaggadia *et al.*,[20] which also improved the accuracy of the numerical solutions for hypersonic flow without a magnetic field. In the present study, the approximation of this parameter between the shock wave and the body is assumed to be linear,

$$\frac{\partial\beta}{\partial\theta} = ar + b \tag{18}$$

here, the coefficients a and b can be derived from the above boundary conditions Eqs. (16) and (17), and Eq. (18) is then shown as below:

$$\frac{\partial\beta}{\partial\theta} = \left(\frac{\partial\beta}{\partial\theta}\right)_b \frac{r}{\Delta} - \left(\frac{\partial\beta}{\partial\theta}\right)_b \frac{R_b}{\Delta}. \tag{19}$$

Thus, the value of the shock curvature parameter $(\frac{\partial\beta}{\partial\theta})_b$ at the shock layer along the stagnation streamline must be determined. Since the 1D model is a simplification of the 2D equations, we also deduce the variable $(\frac{\partial\beta}{\partial\theta})_b$ from the 2D results and this value is equal to $(\frac{\partial\beta}{\partial\theta})_b = 1 - \frac{\partial v}{\partial\theta}$ at the position after the detached shock wave. The relationship between the shock curvature parameter and the non-dimensional shock standoff distance of several 2D calculations is shown in Fig. 10. Twelve estimates were obtained for three attitude heights to determine the flow conditions, and the calculation conditions are displayed in Table I. As shown in Fig. 10, the larger the shock standoff distance, the larger the shock curvature parameter is, which agrees with the trend shown in Fig. 8. Unfortunately, the larger the shock curvature parameter, the more the offset of the bow shock deviates from a concentric sphere. Subsequently, a fitting correlation based

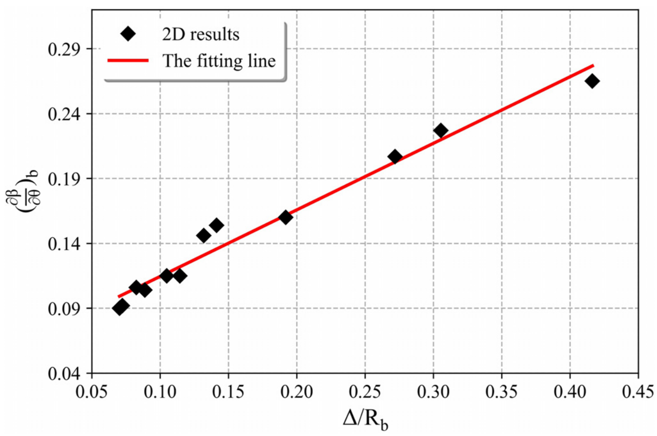

FIG. 10. The relationship between the shock curvature parameter $(\frac{\partial\beta}{\partial\theta})_b$ and the dimensionless shock standoff distance. Twelve estimate points are calculated under three cases in Table I, and the magnetic fields are 0, 0.3, 0.5, and 0.7 T.

on these calculation results is obtained, and the expression is shown in Eq. (20). The variable $(\frac{\partial\beta}{\partial\theta})_b$ is only dependent on the shock stand-off distance Δ and radius of the sphere R_b. It can be used to determine the boundary condition of $(\frac{\partial\beta}{\partial\theta})_b$ in the improved 1D model

$$\left(\frac{\partial\beta}{\partial\theta}\right)_b = 0.5127\frac{\Delta}{R_b} + 0.0633. \tag{20}$$

Notably, although Eq. (20) is deduced from the 2D simulations, it is no longer necessary to run additional 2D simulations in the follow-up actual application of this equation, where the shock stand-off distance Δ in this equation can be obtained directly from 1D simulations. Since the issue that we are concerned with is a steady-state problem, this value tends to be constant as the calculation iterates. Finally, the newly added dependent variable $\frac{\partial\beta}{\partial\theta}$ in Eq. (19) can be obtained by the results of Eq. (20). Moreover, Eq. (20) is an approximate formula, and the shock stand-off distance can also be obtained by some theoretical models in advance, as shown in Ref. 40.

Additionally, although the above correlation is based on the hypersonic MHD flow, the method is generic and may be applied to other hypersonic flows ($B_0 = 0$ T in the present study).

IV. RESULTS AND DISCUSSION

The results with the consideration of the shock curvature parameter are discussed first. These results are referred to as 1D-SC for short. As shown in Fig. 7, it is apparent that the consideration of the shock curvature parameter solves the problem discussed in Sec. II. After making this correction, the tangential velocity gradient shows a reasonable agreement between the 1D-SC and 2D.

The comparisons of the stagnation point heat flux and shock standoff distance between the 1D-SC and 2D are shown in Table III and Fig. 11. Table III indicates that the consideration of the shock curvature parameter has a negligible influence on predicting the stagnation point heat flux. The largest deviation between 1D-SC and 2D is about 3.8%, whereas this value is 3.3% for the 1D results. However, the shock standoff distances of the 1D-SC are significantly improved for

TABLE III. Stagnation point heat flux and shock standoff distance for case 2.

		0 T	0.3 T	0.5 T	0.7 T
Δ (m)	1D-SC	0.092	0.137	0.250	0.4155
	2D	0.095	0.142	0.259	0.412
	Deviation	3.2%	3.5%	3.5%	0.8%
q_w (kW/m^2)	1D-SC	253.16	223.75	210.59	199.94
	2D	263.26	230.16	209.28	200.00
	Deviation	3.8%	2.8%	0.6%	0.1%

all cases. The deviation is within 3.5% for all cases, whereas a deviation of 15.7% existed for the 1D simulation at $B_0 = 0.7$ T.

In addition to the above comparison between 1D, 1D-SC, and 2D for case 2, detailed comparisons are also conducted for the other two cases (case 1 and case 3), as shown in Figs. 12, 13, and Table IV. Figures 12 and 13 show the comparison of the flow properties along the stagnation streamline between 1D-SC and 2D for case 1 ($h = 55.7$ km) and case 3 ($h = 63.6$ km), respectively. The trends of the pressure and translational temperature show an excellent agreement between 1D-SC and 2D for all strengths of the magnetic field. The shock standoff distance and the stagnation point heat flux for 1D-SC and 2D are listed in Table IV. The deviation for the shock standoff distance is within 2.8% for case 1 and case 3, and the deviation for the stagnation point heat flux is within 4.3%. Thus, the proposed 1D-SC method has been validated by the 2D calculation, indicating that the method provides accurate results of the stagnation streamline properties in hypersonic MHD flows.

Finally, we briefly explain the efficiency of the proposed quasi-one-dimensional calculation, which is another primary objective for the hypersonic MHD flow simulation. The central processing unit (CPU) times are approximately 120 h for the 2D simulations in all cases on a recent personal computer, employing the message passing interface (MPI) implementation with eight processors, whereas only

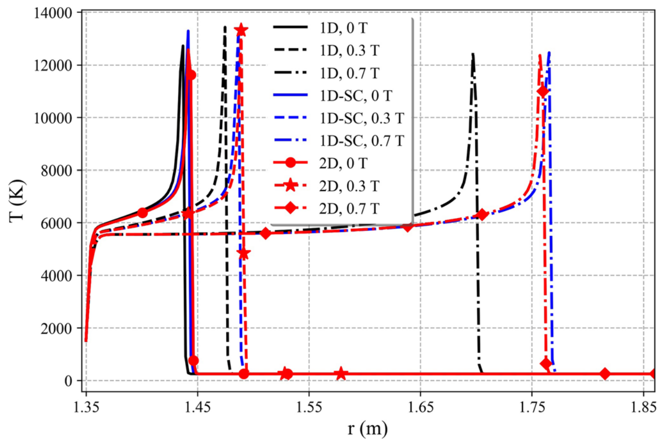

FIG. 11. Comparison of the translational–rotational temperature along the stagnation streamline for case 2.

60 h are required for the quasi-one-dimensional simulations with one processor. Thus, the proposed quasi-one-dimensional method agrees well with the 2D calculations and has high efficiency.

V. CONCLUSION

This work proposed a quasi-one-dimensional model based on the DRNSE to obtain the stagnation streamline properties of a blunt body in hypersonic MHD flows. The Lorentz force term was incorporated into the stagnation streamline model. The proposed model was validated by comparing it with the 2D Navier–Stokes calculations for flows around the OREX model. The original model without the shock curvature correction gives a deviation of the shock standoff distance by about 8.4% at $B_0 = 0$ T (without a magnetic field), and by 5.7% at $B_0 = 0.7$ T. The larger the magnetic field, the larger the shock standoff distance was, and the larger the deviation was. Furthermore, the shock curvature parameter was incorporated into the model, and an

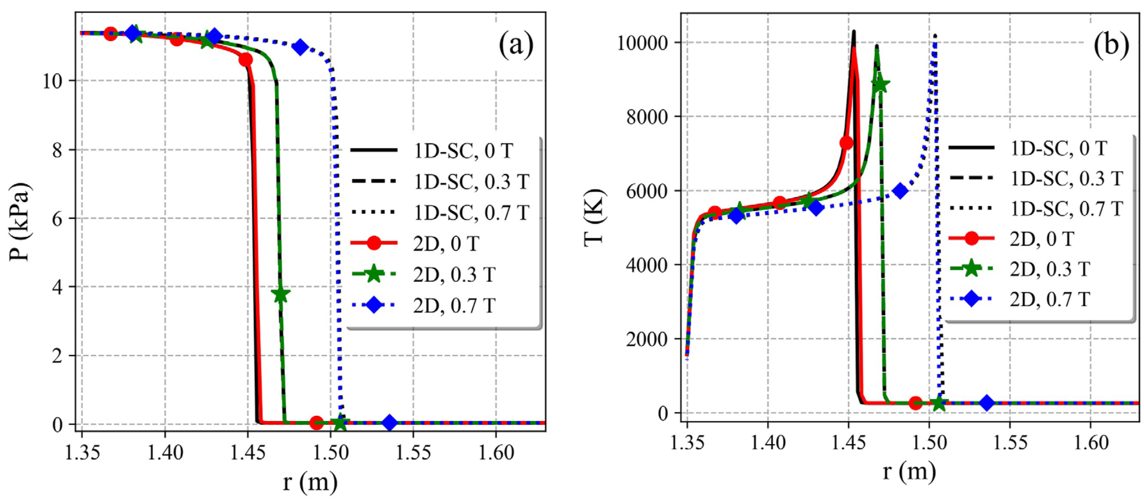

FIG. 12. Comparison of the flow properties along the stagnation streamline between the 1D-SC and 2D simulations for case 1: (a) Pressure and (b) translational–rotational temperature.

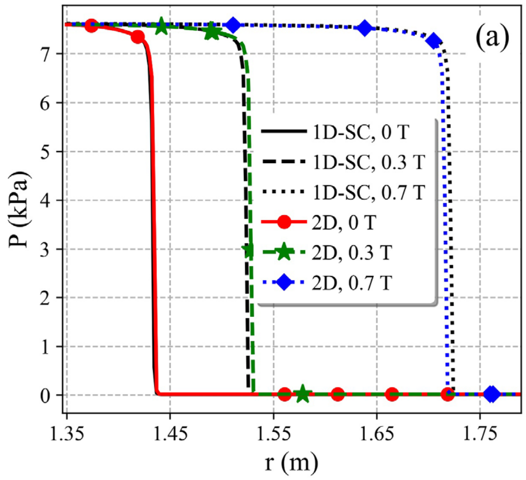

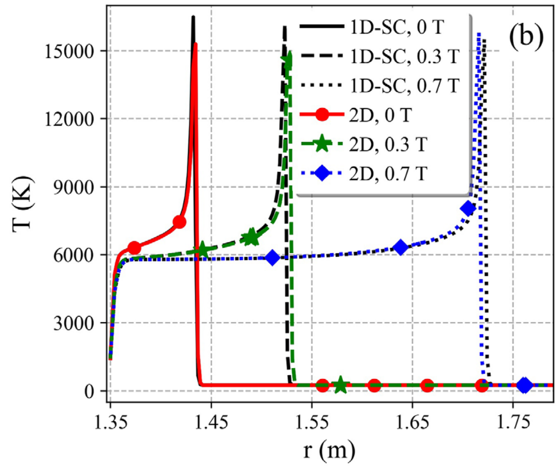

FIG. 13. Comparison of the flow properties along the stagnation streamline between the 1D-SC and 2D simulations for case 3. (a) Pressure and (b) translational–rotational temperature.

TABLE IV. Stagnation point heat flux and shock standoff distance for case 1 and case 3.

		Case 1, $h = 55.7$ km			Case 3, $h = 63.6$ km		
		0 T	0.3 T	0.5 T	0 T	0.3 T	0.5 T
Δ (m)	1D-SC	0.103	0.118	0.154	0.082	0.173	0.372
	2D	0.106	0.120	0.155	0.083	0.178	0.367
	Deviation	2.8%	1.7%	0.6%	1.2%	2.8%	1.4%
q_w (kW/m^2)	1D-SC	197.26	184.70	172.51	273.23	234.76	217.36
	2D	205.15	192.92	176.02	283.96	235.34	218.07
	Deviation	3.8%	4.3%	2.0%	3.8%	0.2%	0.3%

approximate expression deduced from the 2D calculation results was obtained. The results showed that the improved quasi-one-dimensional model significantly improved the prediction accuracy of the shock standoff distance; the deviation was within 3.5% for all cases. In addition, the model has high efficiency to obtain the stagnation streamline properties and provides reasonable results, including the stagnation point heat flux. Since the shock curvature parameter approximation is generic, it can be used in the original DRNSE method for hypersonic flows without the applied magnetic field.

ACKNOWLEDGMENTS

The authors would like to acknowledge Q. Hong for the helpful discussions.

This work was supported by the National Natural Science Foundation of China (Grant Nos. 12072352 and 12232018), and the Youth Innovation Promotion Association CAS (Grant No. 2021020).

AUTHOR DECLARATIONS

Conflict of Interest

The authors have no conflicts to disclose.

Author Contributions

Kai Luo: Conceptualization (lead); Formal analysis (lead); Investigation (lead); Methodology (lead); Software (lead); Validation (lead); Visualization (lead); Writing – original draft (lead); Writing – review & editing (lead). **Qiu Wang:** Funding acquisition (supporting); Project administration (lead); Supervision (lead); Writing – original draft (supporting); Writing – review & editing (supporting). **Jinping Li:** Software (supporting); Writing – original draft (supporting); Writing – review & editing (supporting). **Wei Zhao:** Funding acquisition (supporting); Writing – original draft (supporting). **Sangdi Gu:** Writing – original draft (supporting); Writing – review & editing (supporting).

DATA AVAILABILITY

The data that support the findings of this study are available from the corresponding author upon reasonable request.

APPENDIX A: NONEQUILIBRIUM NAVIER–STOKES EQUATIONS FOR MHD FLOWS

The compressible Navier–Stokes equation with MHD interaction terms based on the low magnetic Reynolds number model, which consists of chemical species, momentum, total energy, and vibrational-electronic-electron energy conservation equations, are used as the governing equations for gas dynamics. Generally, the ionized air produced during hypersonic flow is a poor electrical conductor, and the magnetic field induced by the plasma current is much smaller than the applied magnetic field and diffuses rapidly. Thus, the induced magnetic field is ignored, and a low magnetic Reynolds number is assumed in the present study. Therefore, the governing equations in spherical coordinates (r, θ, φ) for rotationally symmetric flow are defined as follows:

$$\frac{\partial \boldsymbol{Q}}{\partial t} + \frac{\partial \boldsymbol{F}}{\partial r} + \frac{1}{r}\frac{\partial \boldsymbol{G}}{\partial \theta} + \boldsymbol{H} = \frac{\partial \boldsymbol{F}_v}{\partial r} + \frac{1}{r}\frac{\partial \boldsymbol{G}_v}{\partial \theta} + \boldsymbol{H}_v + \boldsymbol{S}_{\text{Flow}} + \boldsymbol{S}_{MHD}. \tag{A1}$$

The vectors in Eq. (A1) are displayed as below:

$$\boldsymbol{Q} = \begin{bmatrix} \rho_s \\ \rho u \\ \rho v \\ E_t \\ E_v \end{bmatrix}, \quad \boldsymbol{F} = \begin{bmatrix} \rho_s u \\ \rho u^2 + p \\ \rho uv \\ (E_t + p)u \\ E_v u \end{bmatrix}, \quad \boldsymbol{G} = \begin{bmatrix} \rho_s v \\ \rho uv \\ \rho v^2 + p \\ (E_t + p)v \\ E_v v \end{bmatrix},$$

$$\boldsymbol{F}_v = \begin{bmatrix} j_{Dr,s} \\ \tau_{rr} \\ \tau_{r\theta} \\ q_r + \tau_{rr}u + \tau_{r\theta}v \\ q_{v,r} \end{bmatrix},$$

$$\boldsymbol{H} = \begin{bmatrix} \frac{2}{r}\rho_s u + \frac{\cot\theta}{r}\rho_s v \\ \frac{2}{r}\rho u^2 + \frac{\cot\theta}{r}\rho uv - \frac{1}{r}\rho v^2 \\ \frac{3}{r}\rho uv + \frac{\cot\theta}{r}\rho v^2 \\ \frac{2}{r}(E_t + p)u + \frac{\cot\theta}{r}(E_t + p)v \\ \frac{2}{r}E_v u + \frac{\cot\theta}{r}E_v v \end{bmatrix}, \tag{A2}$$

$$\boldsymbol{H}_v = \begin{bmatrix} \frac{2}{r}j_{Dr,s} + \frac{\cot\theta}{r}j_{D\theta,s} \\ \frac{2}{r}\tau_{rr} + \frac{\cot\theta}{r}\tau_{r\theta} - \frac{1}{r}\tau_{\theta\theta} - \frac{1}{r}\tau_{\varphi\varphi} \\ \frac{3}{r}\tau_{r\theta} + \frac{\cot\theta}{r}\tau_{\theta\theta} - \frac{\cot\theta}{r}\tau_{\varphi\varphi} \\ \frac{2}{r}(\tau_{rr}u + \tau_{r\theta}v + q_r) + \frac{\cot\theta}{r}(\tau_{r\theta}u + \tau_{\theta\theta}v + q_\theta) \\ \frac{2}{r}q_{v,r} + \frac{\cot\theta}{r}q_{v,\theta} \end{bmatrix},$$

$$\boldsymbol{S}_{\text{Flow}} = \begin{bmatrix} \omega_s \\ 0 \\ 0 \\ 0 \\ S_v \end{bmatrix}, \quad \boldsymbol{G}_v = \begin{bmatrix} j_{D\theta,s} \\ \tau_{r\theta} \\ \tau_{\theta\theta} \\ q_r + \tau_{\theta\theta}v + \tau_{r\theta}u \\ q_{v,\theta} \end{bmatrix},$$

where $\boldsymbol{Q}$ is the vector of the conservative variables. $\boldsymbol{F}$, $\boldsymbol{G}$, and $\boldsymbol{H}$ are the inviscid flux vector; $\boldsymbol{F}_v$, $\boldsymbol{G}_v$, and $\boldsymbol{H}_v$ are the viscous flux vector; $\boldsymbol{S}_{\text{Flow}}$ is the chemical source term. t is time; r and θ are the radial and polar coordinates of the physical space in Eq. (A1), respectively. Compared to the standard conservation equations without a magnetic field, only a source term associated with the MHD effects is added in the above equation, i.e., $\boldsymbol{S}_{MHD}$ as shown in the equation:

$$\boldsymbol{S}_{MHD} = \begin{bmatrix} 0 \\ (\boldsymbol{J} \times \boldsymbol{B})_r \\ (\boldsymbol{J} \times \boldsymbol{B})_\theta \\ \boldsymbol{J} \cdot \boldsymbol{E} \\ \frac{\boldsymbol{J} \cdot \boldsymbol{J}}{\sigma} \end{bmatrix}, \tag{A3}$$

where $\boldsymbol{J} \times \boldsymbol{B}$ is the Lorentz force in the momentum equation, and $\frac{\boldsymbol{J} \cdot \boldsymbol{J}}{\sigma}$ is the Joule dissipation term in the vibrational-electronic-electron energy equation. σ is the electrical conductivity. $\boldsymbol{J}$ is the electric current density vector; $\boldsymbol{E}$ is the electric strength vector; and $\boldsymbol{B}$ is the magnetic induction vector. The current density $\boldsymbol{J}$ is calculated by the generalized Ohm's law,

$$\boldsymbol{J} = \sigma(\boldsymbol{E} + \boldsymbol{U} \times \boldsymbol{B}). \tag{A4}$$

Although some studies have been carried out on the Hall effect of hypersonic MHD flow, there are still great uncertainties in the influence of the qualitative/quantitative law of the Hall effect.[41] To simplify the equations and achieve a high-efficiency one-dimensional model for MHD flows, we assume an axisymmetric two-dimensional electromagnetic field and ignore the Hall and ion slip in the present paper like most scholars. Thus, the electric field $\boldsymbol{E}$ in Eq. (A3) is zero. Consequently, the electric current density has only the azimuthal (φ) component, which is written as follows:

$$J_\varphi = \sigma(uB_\theta - vB_r). \tag{A5}$$

Since we are dealing with rotationally symmetric problems, we can assume that $w = 0$, $B_\varphi = 0$, and $\frac{\partial}{\partial \varphi} = 0$. Therefore, $\boldsymbol{S}_{MHD}$ can be simplified as follows:

$$\boldsymbol{S}_{MHD} = \begin{bmatrix} 0 \\ -\sigma B_\theta(uB_\theta - vB_r) \\ \sigma B_r(uB_\theta - vB_r) \\ 0 \\ \frac{\boldsymbol{J} \cdot \boldsymbol{J}}{\sigma} \end{bmatrix}. \tag{A6}$$

In the above equations, the total mass density ρ and the total specific energy E_t are given by

$$\rho = \sum_s \rho_s, \quad E_t = \rho e + \rho \boldsymbol{U}^2/2, \tag{A7}$$

where ρ_s and $j_{D,s}$ represent the density and the diffusion fluxes of species s, respectively. u and v are the velocity components in the r

and θ directions, respectively. E_v is the vibrational energy. q_r, q_θ, $q_{v,r}$, and $q_{v,\theta}$ are the total heat flux and vibrational heat flux in the r and θ direction, respectively. ω_s and S_v represent the mass production rate of species s and the mass production rate of the vibrational energy, respectively. The expressions of these variables are available in Refs. 34 and 42. The elements of the stress tensor are obtained from Ref. 24.

APPENDIX B: ELECTRICAL CONDUCTIVITY

The electrical conductivity is required to calculate the current density from the generalized Ohm's law. Here, the electrical conductivity was estimated based on the common relationship using the cross-sectional integral for electrons, as defined in the following equation:

$$\sigma = \frac{n_e e^2}{m_e \sum_{s\neq e} \nu_{e,s}^m}. \tag{B1}$$

The effective energy exchange collision frequency $\nu_{e,s}^m$ of electrons with the other chemical species s is calculated using the following equation:

$$\nu_{e,s}^m = \begin{cases} \frac{4}{3}\sigma_{e,s}^m n_s \sqrt{\frac{8k_bT_e}{\pi m_e}}, & s = \text{ions}, \\ 6\pi\left(\frac{e^2}{12\pi\varepsilon_0 k_b T_e}\right)^2 \cdot ln\left[12\pi\left(\frac{\varepsilon_0 k_b}{e^2}\right)^{1.5}\sqrt{\frac{T_e^3}{n_e}}\right] & \\ \times n_s\sqrt{\frac{8k_bT_e}{\pi m_e}}, & s \neq \text{ions}, \end{cases} \tag{B2}$$

where $\sigma_{e,s}^m$ represents the effective energy exchange cross section of the electrons with the neutral species and is computed using the curve fitting method presented in Ref. 34. k_b and ε_0 are the Boltzmann constant and vacuum dielectric constant, respectively. Here e, m_e, n_e, and n_s are the electron charge, electron mass, electron number density, and the number density of the chemical species s, respectively. The electron temperature T_e is equal to the vibrational temperature T_v according to Park's two-temperature model used in the present study.

APPENDIX C: VECTORS IN THE QUASI-ONE-DIMENSIONAL EQUATION

The vector $\boldsymbol{Q}$, $\boldsymbol{F}$, $\boldsymbol{H}$, $\boldsymbol{F_v}$, $\boldsymbol{H_v}$, $\boldsymbol{S}_{\text{Flow}}$, and $\boldsymbol{S}_{MHD}$ can be derived from Eqs. (3), (9) and (A2), which are written as follows:

$$\boldsymbol{Q} = \begin{bmatrix} \rho_s \\ \rho u_1 \\ \rho v_1 \\ E_t \\ E_v \end{bmatrix}, \quad \boldsymbol{F} = \begin{bmatrix} \rho_s u_1 \\ \rho u_1^2 + p_1 + p_\infty \\ \rho u_1 v_1 \\ (E_t + p_1 + p_\infty)u_1 \\ E_v u_1 \end{bmatrix}, \quad \boldsymbol{F}_v = \begin{bmatrix} j_{Dr,s} \\ \bar{\tau}_{rr} \\ \bar{\tau}_{r\theta} \\ q_r + \bar{\tau}_{rr}u_1 \\ q_{v,r} \end{bmatrix},$$

$$\boldsymbol{S}_{MHD} = \begin{bmatrix} 0 \\ -\sigma B_\theta(u_1\cos\theta B_\theta - v_1 \sin\theta B_r) \\ \dfrac{\sigma B_r(u_1\cos\theta B_\theta - v_1\sin\theta B_r)}{\sin\theta} \\ 0 \\ \dfrac{\boldsymbol{J}\cdot\boldsymbol{J}}{\sigma} \end{bmatrix},$$

$$\boldsymbol{H} = \begin{bmatrix} \frac{2}{r}\rho_s(u_1+v_1) \\ \frac{2}{r}\rho\left(u_1^2 + u_1 v_1\right) \\ \frac{3}{r}\rho\left(v_1^2 + u_1v_1\right) - \frac{2}{r}p_1 - \frac{1}{r\sin\theta}\int_r^{r_\infty}\frac{\partial F_{L,r}}{\partial\theta}dr \\ \frac{2}{r}(E_t + p_1 + p_\infty)(u_1+v_1) \\ \frac{2}{r}E_v(u_1+v_1) \end{bmatrix}, \tag{C1}$$

$$\boldsymbol{H_v} = \begin{bmatrix} \frac{2}{r}j_{Dr,s} \\ \frac{2}{r}\left(\bar{\tau}_{rr} + \bar{\tau}_{r\theta} - \frac{1}{2}\bar{\tau}_{\theta\theta} - \frac{1}{2}\bar{\tau}_{\varphi\varphi}\right) \\ \frac{3}{r}\bar{\tau}_{r\theta} - \frac{1}{r}\bar{\tau}_{\theta\theta} \\ \frac{2}{r}(q_r + \bar{\tau}_{rr}u_1 + \bar{\tau}_{r\theta}u_1 + \bar{\tau}_{\theta\theta}v_1) \\ \frac{2}{r}q_{v,r} \end{bmatrix}, \quad \boldsymbol{S}_{\text{Flow}} = \begin{bmatrix} \omega_s \\ 0 \\ 0 \\ 0 \\ S_v \end{bmatrix},$$

where the stress tensors τ_{rr}, $\tau_{r\theta}$, $\tau_{\theta\theta}$, $\tau_{\varphi\varphi}$ were changed into $\bar{\tau}_{rr}$, $\bar{\tau}_{r\theta}$, $\bar{\tau}_{\theta\theta}$, $\bar{\tau}_{\varphi\varphi}$ as follows:

$$\begin{aligned} \bar{\tau}_{rr} &= \frac{\tau_{rr}}{\cos\theta} = \mu\left(\frac{4}{3}\frac{\partial u_1}{\partial r} - \frac{4}{3}\frac{u_1}{r} - \frac{4}{3}\frac{v_1}{r}\right), \\ \bar{\tau}_{r\theta} &= \frac{\tau_{r\theta}}{\sin\theta} = \mu\left(-\frac{v_1}{r} - \frac{\partial v_1}{\partial r} - \frac{u_1}{r}\right), \\ \bar{\tau}_{\theta\theta} = \bar{\tau}_{\varphi\varphi} &= \frac{\tau_{\theta\theta}}{\cos\theta} = \mu\left(-\frac{2}{3}\frac{\partial v_1}{\partial r} + \frac{2}{3}\frac{u_1}{r} + \frac{2}{3}\frac{v_1}{r}\right) \end{aligned} \tag{C2}$$

here, μ is the mixture viscosity coefficient.

APPENDIX D: VECTORS IN THE IMPROVED QUASI-ONE-DIMENSIONAL EQUATION

The components of the inviscid flux $\boldsymbol{H}$, the viscous flux vectors $\boldsymbol{H_v}$, and the source term $\boldsymbol{S}_{MHD}$ in Eq. (11) are corrected from Eqs. (13), (15) and (C1), which are shown as follows:

$$H = \begin{bmatrix} \frac{2}{r}\rho_s u_1 + \frac{2}{r}\left(1 - \frac{\partial\beta}{\partial\theta}\right)\rho_s v_1 \\ \frac{2}{r}\rho u_1^2 + \frac{2}{r}\rho\left(1 - \frac{\partial\beta}{\partial\theta}\right)u_1 v_1 \\ \frac{3}{r}\rho\left(u_1v_1 + {v_1}^2\right) - \frac{2}{r}\left(1 - \frac{\partial\beta}{\partial\theta}\right)p_1 - \frac{1}{r\sin(\theta-\beta)}\int_r^{r_\infty}\frac{\partial F_{L,r}}{\partial\theta}dr \\ \frac{2}{r}(E_t + p_1 + p_\infty)u_1 + \frac{2}{r}\left(1 - \frac{\partial\beta}{\partial\theta}\right)(E_t + p_1 + p_\infty)v_1 \\ \frac{2}{r}E_v u_1 + \frac{2}{r}E_v\left(1 - \frac{\partial\beta}{\partial\theta}\right)v_1 \end{bmatrix},$$

$$H_{\mathbf{v}} = \begin{bmatrix} \frac{2}{r} j_{Dr,s} \\ \frac{2}{r}\bar{\tau}_{rr} + \frac{2}{r}\left(1 - \frac{\partial \beta}{\partial \theta}\right)\bar{\tau}_{r\theta} - \frac{1}{r}\bar{\tau}_{\theta\theta} - \frac{1}{r}\bar{\tau}_{\varphi\varphi} \\ \frac{3}{r}\bar{\tau}_{r\theta} - \frac{1}{r}\left(1 - \frac{\partial \beta}{\partial \theta}\right)\bar{\tau}_{\theta\theta} \\ \frac{2}{r} q_r + \frac{2}{r}\bar{\tau}_{rr} u_1 + \frac{2}{r}\left(1 - \frac{\partial \beta}{\partial \theta}\right)\bar{\tau}_{r\theta} u_1 \\ + \frac{2}{r}\left(1 - \frac{\partial \beta}{\partial \theta}\right)\bar{\tau}_{\theta\theta} v_1 \\ \frac{2}{r} q_{v,r} \end{bmatrix}, \tag{D1}$$

$$S_{\mathbf{MHD}} = \begin{bmatrix} 0 \\ -\sigma B_\theta (u_1 \cos(\theta - \beta) B_\theta - v_1 \sin(\theta - \beta) B_r) \\ \frac{\sigma B_r (u_1 \cos(\theta - \beta) B_\theta - v_1 \sin(\theta - \beta) B_r)}{\sin(\theta - \beta)} \\ 0 \\ \frac{\boldsymbol{J} \cdot \boldsymbol{J}}{\sigma} \end{bmatrix}.$$

APPENDIX E: VALIDATION TESTS FOR TWO-DIMENSIONAL MHD MODEL

To show the utility of the two-dimensional MHD model for solving laminar, hypersonic MHD flows, we performed extensive verification and validation.

1. Theory solution for shock standoff distance

The model is first reduced to its inviscid Euler equivalent, closed with an ideal gas equation of state for comparison with the validation test cases in the literature.[5] This validation test for a hypersonic MHD system under low magnetic Reynolds number assumption is the theoretical test proposed by Poggie and Gaitonde.[5] It has also been replicated subsequently by Damevin and Hoffmann,[43] and Fujino *et al.*[44] The corresponding dimensional conditions are a sphere of 10 mm radius. The freestream temperature is 100 K, where the velocity and static pressure are 1002.25 m/s and 2290.85 Pa, respectively. The magnetic field is a static imposed dipole field as shown in Eq. (12). The MHD effect is shown to increase shock standoff distance with increased magnetic interaction parameter defined as follows:

$$Q = \frac{\sigma B_0^2 R_b}{\rho_\infty U_\infty}, \tag{E1}$$

where σ is taken to be a constant conductivity of $\sigma = 300$ S/m in the post-shock region. For hypersonic MHD flows, the magnetic interaction parameter Q, rather than the Mach number or Reynolds number commonly used in fluid dynamics, is frequently used to estimate the MHD effect. Q represents the relationship between the Lorentz force and the Fluid inertial force, as shown in Eq. (E1). MHD effects become significant for $Q > 1$.

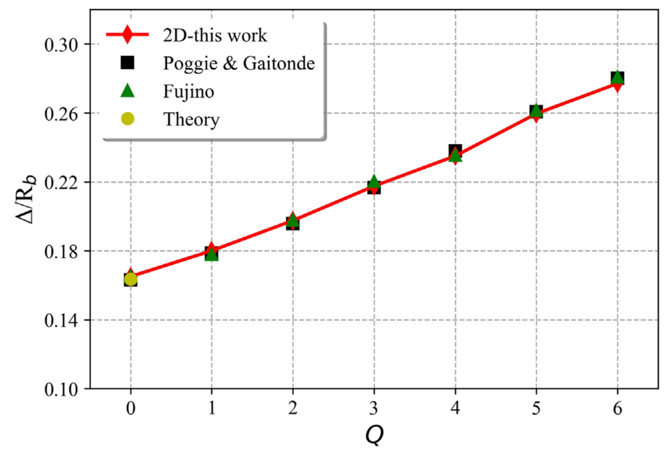

FIG. 14. Comparison of shock standoff distance for this work vs previous studies for $Q = 0 - 6$.

Variation of the shock stand-off distance with Q is shown in Fig. 14, which exhibits excellent agreement with literature results and theory.

2. Hypersonic cylinder experiments

The high enthalpy flow past a cylinder performed in HEG[45] is also chosen to validate our thermochemical nonequilibrium model. The specific total enthalpy of the freestream amounts to 13.4 MJ/kg and the flow conditions are given as $M = 8.78$, $T = 694$ K and $P = 687$ Pa, and the diameter of the cylinder is 90 mm. The isothermal and fully catalytic wall boundary conditions are adopted for the cylinder surface with $T_w = 300$ K. Figure 15 exhibits the comparison of the measured and numerical surface heat flux, which shows that the two-dimensional numerical code used in this paper can predict the surface heat flux accurately considering the thermal and chemical nonequilibrium effects.

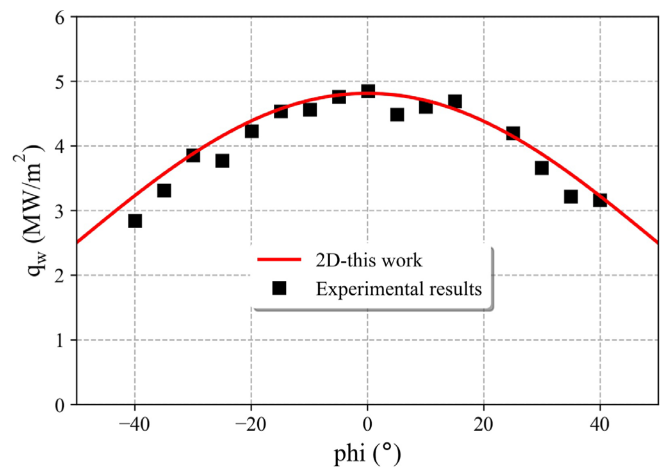

FIG. 15. Comparison of the measured and numerical result of surface heat flux distribution.

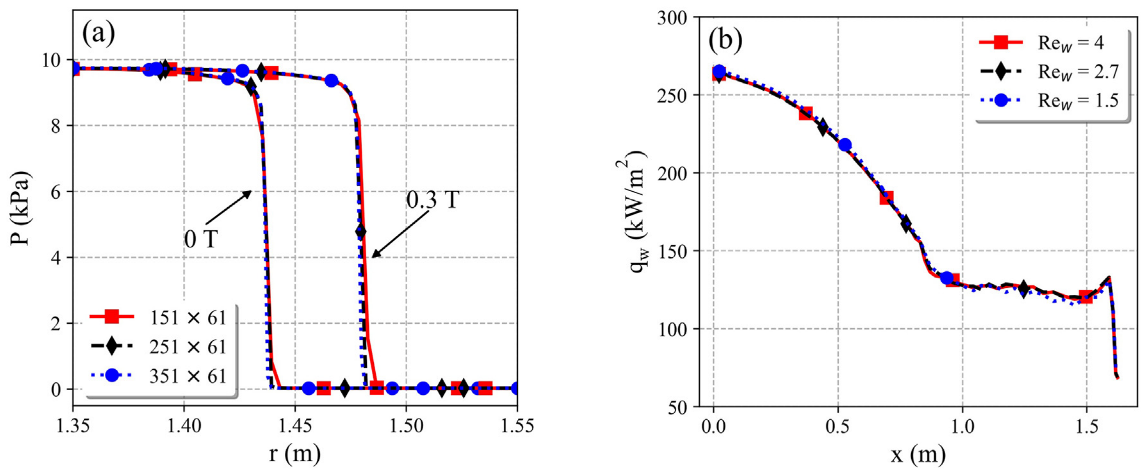

FIG. 16. Grid resolution analysis results for case 2: (a) Pressure at the stagnation streamline for the 2D simulation and (b) heat flux on the wall for the 2D simulation with a grid resolution of 251 $\times$ 61.

APPENDIX F: GRID INDEPENDENCE STUDY

The surface heat flux and the shock standoff distance are the key parameters to study in the MHD flow around a blunt body, and the sensitivity of these two parameters to the grid scale is different. A grid convergence study for the 2D calculation is conducted to calculate the shock standoff distance using the numerical methods with three different grid resolutions (151 $\times$ 61, 251 $\times$ 61, and 351 $\times$ 61 grid points, where the first numbers represent the grid nodes along the radial coordinate). The simulations are performed for case 2. We observed a negligible difference in the pressure on the stagnation line or the shock standoff distance between the three grid resolutions, as shown in Fig. 16(a). Thus, the mesh size of 251 $\times$ 61 is employed for the 2D computation. The surface heat flux is often more sensitive to the grid scale, especially near the wall surface. As a rule of thumb for predicting the surface heat flux, various computational scientists have stated the importance of the wall cell Reynolds number,[46]

$$Re_w = \frac{\rho_w a_w \Delta x}{\mu_w}, \tag{F1}$$

where Δx is the size of the first cell next to the wall. μ_w and a_w are the mixture viscosity coefficient and the sound speed at the wall. Zones near the wall are incorporated with clustered points and Re_w is changed with different grid resolutions next to the wall. As shown in Fig. 16(b), there was a negligible difference in the wall heat flux for the three wall cell Reynolds number. The same grid scale along the radial coordinate is chosen both for the 1D and 2D calculations in the following analysis, which also facilitates comparing the results. Finally, 251 grid nodes are used along the radial coordinate, where $Re_w = 2.7$ and the first cell size next to the wall is 1 $\times 10^{-5}$ m.

REFERENCES

[1]E. Resler, Jr. and W. R. Sears, "The prospects for magneto-aerodynamics," J. Aerosp. Sci. **25**, 235–245 (1958).
[2]W. B. Bush, "Magnetohydrodynamic-hypersonic flow past a blunt body," J. Aerosp. Sci. **25**, 685–690 (1958).
[3]R. W. Ziemer and W. B. Bush, "Magnetic field effects on bow shock stand-off distance," Phys. Rev. Lett. **1**, 58 (1958).
[4]G. Ludford and J. D. Murray, "On the flow of a conducting fluid past a magnetized sphere," J. Fluid Mech. **7**, 516–528 (1960).
[5]J. Poggie and D. V. Gaitonde, "Magnetic control of flow past a blunt body: Numerical validation and exploration," Phys. Fluids **14**, 1720–1731 (2002).
[6]Y. Takizawa, S. Sato, T. Abe, and D. Konigorski, "Electro-magnetic effect on shock layer structure in reentry-related high-enthalpy flow," AIAA Paper No. 2004-2162, 2004, p. 2162.
[7]A. Gülhan, B. Esser, U. Koch, F. Siebe, J. Riehmer, D. Giordano, and D. Konigorski, "Experimental verification of heat-flux mitigation by electromagnetic fields in partially-ionized-argon flows," J. Spacecr. Rockets **46**, 274–283 (2009).
[8]A. Cristofolini, C. Borghi, G. Neretti, F. Battista, A. Schettino, E. Trifoni, F. De Filippis, A. Passaro, and D. Baccarella, "MHD interaction around a blunt body in a hypersonic unseeded air flow: Experimental results and numerical rebuilding," AIAA Paper No. 2012-5804, 2012, p. 5804.
[9]A. Lefevre, D. E. Gildfind, R. J. Gollan, P. A. Jacobs, T. J. McIntyre, and C. M. James, "Expansion tube experiments of magnetohydrodynamic aerobraking for superorbital earth reentry," AIAA J. **59**, 3228–3240 (2021).
[10]D. E. Gildfind, D. Smith, A. Lefevre, P. A. Jacobs, and T. J. McIntyre, "Magnetohydrodynamic aerobraking shock stand-off measurements with flight representative electrodynamic boundary conditions," AIAA J. **60**, 41–55 (2022).
[11]A. Lefevre, D. Gildfind, R. Gollan, P. Jacobs, T. McIntyre, and C. M. James, "Experimental study of total heat flux mitigation using magnetohydrodynamic flow control in superorbital earth reentry flight," AIAA Paper No. 2022-0828, 2022, p. 0828.
[12]M. Brio and C. C. Wu, "An upwind differencing scheme for the equations of ideal magnetohydrodynamics," J. Comput. Phys. **75**, 400–422 (1988).
[13]S.-H. Han, J.-I. Lee, and K. H. Kim, "Accurate and robust pressure weight advection upstream splitting method for magnetohydrodynamics equations," AIAA J. **47**, 970–981 (2009).
[14]G. Zha, Y. Shen, and B. Wang, "An improved low diffusion E-CUSP upwind scheme," Comput. Fluids **48**, 214–220 (2011).
[15]Z. Zhou, Z. Zhang, Z. Gao, K. Xu, and C.-H. Lee, "Numerical investigation on mechanisms of mhd heat flux mitigation in hypersonic flows," Aerospace **9**, 548 (2022).
[16]H. A. Muir and N. Nikiforakis, "Numerical modeling of imposed magnetohydrodynamic effects in hypersonic flows," Phys. Fluids **34**, 107114 (2022).
[17]H. Olivier, "A theoretical model for the shock stand-off distance in frozen and equilibrium flows," J. Fluid Mech. **413**, 345–353 (2000).
[18]C. Y. Wen and H. G. Hornung, "Non-equilibrium dissociating flow over spheres," J. Fluid Mech. **299**, 389–405 (1995).

[19]H. G. Hornung, "Non-equilibrium dissociating nitrogen flow over spheres and circular cylinders," J. Fluid Mech. **53**, 149–176 (1972).
[20]N. Belouaggadia, H. Olivier, and R. Brun, "Numerical and theoretical study of the shock stand-off distance in non-equilibrium flows," J. Fluid Mech. **607**, 167–197 (2008).
[21]S. Chen and Q. H. Sun, "A quasi-one-dimensional model for hypersonic reactive flow along the stagnation streamline," Chin. J. Aeronaut. **29**, 1517–1526 (2016).
[22]Q. Z. Hong, X. Y. Wang, Y. Hu, and Q. H. Sun, "Development of a stagnation streamline model for thermochemical nonequilibrium flow," Phys. Fluids **32**, 046102 (2020).
[23]H. C. Kao, "Hypersonic viscous flow near the stagnation streamline of a blunt body. I. A test of local similarity," AIAA J. **2**, 1892–1897 (1964).
[24]A. Klomfass and S. Müller, "Calculation of stagnation streamline quantities in hypersonic blunt body flows," Shock Waves **7**, 13–23 (1997).
[25]J. William, J. Vérant, and P. Sagnier, "An efficient numerical tool for blunted bodies stagnation line rebuilding with weakly ionized thermochemical non-equilibrium flows," in *Proceedings of the 15th IMACS-World Congress on Scientific Computation, Modeling and Applied Mathematics* (Information Scientifique et Technique et Publications, 1997).
[26]C. Lee, "Flow field analysis on the stagnation streamline of a blunt body," Int. J. Aeronaut. Space Sci. **17**, 149–156 (2016).
[27]S. Peng, K. Jin, and X. Zheng, "Study on validity of low-magnetic-Reynolds-number assumption for hypersonic magnetohydrodynamic control," AIAA J. **60**, 6536–6547 (2022).
[28]J. D. Anderson, *Hypersonic and High Temperature Gas Dynamics*, 2nd ed., AIAA Education Series (AIAA, 2006).
[29]M. G. Dunn and S. Kang, "Theoretical and experimental studies of reentry plasmas," Technical Report No. NASA-CR-2232 (NASA, 1973).
[30]C. Park, "Assessment of two-temperature kinetic model for ionizing air," J. Thermophys. Heat Transfer **3**, 233–244 (1989).
[31]F. G. Blottner, M. Johnson, and M. Ellis, "Chemically reacting viscous flow program for multi-component gas mixtures," Technical Report No. SC-RR-70-754 (Sandia Labs, Albuquerque, NM, 1971).
[32]C. Wilke, "A viscosity equation for gas mixtures," J. Chem. Phys. **18**, 517–519 (1950).
[33]G. H. Furumoto, X. Zhong, and J. C. Skiba, "Numerical studies of real-gas effects on two-dimensional hypersonic shock-wave/boundary-layer interaction," Phys. Fluids **9**, 191–210 (1997).
[34]P. A. Gnoffo, *Conservation Equations and Physical Models for Hypersonic Air Flows in Thermal and Chemical Nonequilibrium* (National Aeronautics and Space Administration, Office of Management, 1989), Vol. 2867.
[35]Y. Li, Q. Wang, K. Luo, and W. Zhao, "Formation of bow shock waves around a blunt body in magnetohydrodynamics flows," J. Spacecr. Rockets **59**, 1372–1379 (2022).
[36]K. H. Kim, C. Kim, and O.-H. Rho, "Methods for the accurate computations of hypersonic flows. I. Ausmpw+ scheme," J. Comput. Phys. **174**, 38–80 (2001).
[37]A. Jameson and S. Yoon, "Lower-upper implicit schemes with multiple grids for the Euler equations," AIAA J. **25**, 929–935 (1987).
[38]T. Fujino and M. Ishikawa, "Numerical simulation of control of plasma flow with magnetic field for thermal protection in earth reentry flight," IEEE Trans. Plasma Sci. **34**, 409–420 (2006).
[39]T. Tanifuji, A. Matsuda, K. Wasai, H. Otsu, H. Yamasaki, D. Konigorski, and T. Abe, "Expansion tube experiment of applied magnetic field effect on reentry plasma," AIAA Paper No. 2008-1113, 2008, p. 1113.
[40]Y. Li, Q. Wang, K. Luo, J. Li, and W. Zhao, "Theoretical analysis on hypersonic mhd shock stand-off distance of blunt body," Chin. J. Theor. Appl. Mech. **53**, 2493–2500 (2021).
[41]M. S. Ding, Y. A. Fu, T. S. Gao, D. W. Zhong, J. Tao, and L. Q. Zong, "Influence of hall effect on hypersonic magnetohydrodynamic control," Acta Phys. Sin. **69**, 214703 (2020).
[42]X. D. Li, Z. M. Hu, and Z. L. Jiang, "Numerical investigation on the thermal protection mechanism for blunt body with forward-facing cavity," Sci. China Technol. Sci. **59**, 1120–1129 (2016).
[43]H.-M. Damevin and K. A. Hoffmann, "Numerical simulations of magnetic flow control in hypersonic chemically reacting flows," J. Thermophys. Heat Transfer **16**, 498–507 (2002).
[44]T. Fujino, T. Yoshino, and M. Ishikawa, "Numerical analysis of reentry trajectory coupled with magnetohydrodynamics flow control," J. Spacecr. Rockets **45**, 911–920 (2008).
[45]J. M. Schramm, K. Hannemann, W. Beck, and S. Karl, "Cylinder shock layer density profiles measured in high enthalpy flows in heg," AIAA Paper No. 2002-2913, 2002, p. 2913.
[46]X. Ren, J. Yuan, B. He, M. Zhang, and G. Cai, "Grid criteria for numerical simulation of hypersonic aerothermodynamics in transition regime," J. Fluid Mech. **881**, 585–601 (2019).